Research Article

Lysyl oxidase-like 1 deficiency alters ultrastructural and biomechanical properties of the peripapillary sclera in mice

Lauren K. Wareham [a], John Kuchtey [a], Hang-Jing Wu [a], Evan Krystofiak [b], Yusheng Wu [c], Cynthia A. Reinhart-King [c] and Rachel W. Kuchtey [a,d]*

***a* - Vanderbilt Eye Institute,** *Department of Ophthalmology and Visual Sciences, Vanderbilt University Medical Center, Nashville, TN, USA*

***b* - Cell Imaging Shared Resource,** *Vanderbilt University, Nashville, TN, USA*

***c* - Department of Biomedical Engineering,** *Vanderbilt University, Nashville, TN, USA*

***d* - Department of Molecular Physiology and Biophysics,** *Vanderbilt University, Nashville, TN, USA*

Correspondence to Rachel W. Kuchtey: Vanderbilt Eye Institute, 2311 Pierce Avenue, Nashville, Tennessee 37232, USA. *rachel.w.kuchtey@vumc.org (R.W. Kuchtey)*
https://doi.org/10.1016/j.mbplus.2022.100120

Abstract

Lysyl oxidase-like 1 encoded by the *LOXL1* gene is a member of the lysyl oxidase family of enzymes that are important in the maintenance of extracellular matrix (ECM)-rich tissue. LOXL1 is important for proper elastic fiber formation and mice lacking LOXL1 ($Loxl1^{-/-}$) exhibit systemic elastic fiber disorders, such as pelvic organ prolapse, a phenotype associated with exfoliation syndrome (XFS) in humans. Patients with XFS have a significant risk of developing exfoliation glaucoma (XFG), a severe form of glaucoma, which is a neurodegenerative condition leading to irreversible blindness if not detected and treated in a timely fashion. Although $Loxl1^{-/-}$ mice have been used extensively to investigate mechanisms of pelvic organ prolapse, studies of eyes in those mice are limited and some showed inconsistent ocular phenotypes. In this study we demonstrate that $Loxl1^{-/-}$ mice have significant anterior segment biometric abnormalities which recapitulate some human XFS features. We then focused on the peripapillary sclera (PPS), a critical structure for maintaining optic nerve health. We discovered quantitative and qualitive changes in ultrastructure of PPS, such as reduced elastic fibers, enlarged collagen fibrils, and transformed collagen lamella organization detected by transmission electron microscopy (TEM). Importantly, these changes corelate with altered tissue biomechanics detected by Atomic Force Microscopy (AFM) of PPS in mice. Together, our results support a crucial role for LOXL1 in ocular tissue structure and biomechanics, and $Loxl1^{-/-}$ mice could be a valuable resource for understanding the role of scleral tissue biomechanics in ocular disease.

Introduction

The Lysyl oxidase family consists of 5 members each of which is encoded by a separate gene, Lysl Oxidase (*LOX*) and Lysyl Oxidase-like 1 – 4 (*LOXL1 – 4*) [1]. Lysyl oxidase-like 1 (LOXL1) encoded by the *LOXL1* gene plays an important role in the maintenance of extracellular matrix (ECM)-rich tissue [2,3]. LOXL1 is secreted in the endoplasmic reticulum as a pro-enzyme, where it remains inactive until it reaches elastin-rich tissue [4]. Upon cleavage by bone morphogenetic protein-1 [5], the active form of LOXL1 catalyzes the first step in crosslink formation in elastin and collagen [2,6,7]. LOXL1 is necessary for the proper formation and stability of elastic fibers [6]. As such, LOXL1 is

Nomenclature

ACD	Anterior chamber depth
AFM	Atomic force microscopy
AL	Axial length
CCT	Central corneal thickness
ECM	Extracellular matrix
IOP	Intraocular pressure
LC	Lamina cribrosa
LOXL1	Lysyl oxidase-like 1
SD-OCT	Spectral domain optical coherence tomography
ONH	Optic nerve head
PPS	Peripapillary sclera
PDMS	Polydimethylsiloxane
RGC	Retinal ganglion cell
TEM	Transmission electron microscopy
XFG	Exfoliation glaucoma
XFS	Exfoliation syndrome

expressed in many elastic tissues that constantly undergo cycles of mechanical stretch and repair, including aorta, lung, and uterus [7–10]. *LOXL1* genomic variants are strongly associated with exfoliation syndrome (XFS) [11–16], a systemic disorder of elastic fibers affecting many organs including brain, heart, lung, skin, pelvic floor, and eye [17–20]. In the eye, XFS manifests as the deposition of exfoliation material composed of ECM-rich proteins, including LOXL1 [19]. Patients with XFS are at high risk of developing exfoliation glaucoma (XFG), a blinding neurodegenerative disease [21,22], however, the precise role of LOXL1 in XFS pathophysiology remains unknown.

The eye contains many elastin- and collagen-rich tissues that undergo continuous mechanical stretch and strain, including the sclera. The sclera is important for maintaining eye structure, including the optic nerve which exits the eye through the optic nerve head (ONH) [23]. In humans the supporting connective tissue of the ONH is largely composed of the lamina cribrosa (LC) and peripapillary sclera (PPS). The LC and PPS are both rich in elastic fibers, collagen, and other ECM proteins that form a dense scaffold to support the retinal ganglion cell (RGC) axons as they exit the globe to form the optic nerve [24,25]. Both the LC and PPS undergo constant remodeling responding to constant change of external pressure and intraocular pressure (IOP). Elevated IOP is one of the most significant risk factors for RGC damage [26]. Within the ONH, tight regulation of translaminar pressure in the LC and hoop stress exerted on PPS by IOP is crucial in maintaining the RGC axon health [27]. Notably, the initial site of axonal damage associated with glaucoma is at the ONH [26]. Unlike humans, the mouse ONH does not have collagenous LC [28], and instead astrocytes extend their processes across the ONH to support RGC axons [29]. In mice, the PPS makes contact with the astrocyte basement membrane and the pia mater, thus IOP-generated hoop stress from PPS is transmitted to the ONH via these points of contact [29]. In the PPS, the predominant collagen is type I collagen (>95 %), with collagen types III, V, and VI making up the remaining 5 % [30,31]. Collagen fibrils in the PPS assemble into interwoven bundles called scleral lamellae that give rise to increased tensile strength [32]. Mature elastic fibers consisting of an amorphous elastin core ensheathed by a scaffold of fibrillin-rich microfibrils are found interlaced between collagen lamellae, particularly at the ONH, where elasticity is also crucial [23,33,34].

Multiple changes in ECM-rich tissues can occur with increasing age or with disease, including increased deposition of collagen I, III, and IV, and remodeling of the ECM components due to dysfunction or loss of enzyme activity [35–38]. In this study we utilized Transmission Electron Microscopy (TEM) and Atomic Force Microscopy (AFM) to determine the impact of LOXL1 deficiency on the ultrastructure and stiffness of the PPS in *Loxl1*-deficient mice ($Loxl1^{-/-}$)[6] at an advanced age. Here we report that $Loxl1^{-/-}$ mice have biometric changes of the anterior segment of the eye and lower visual acuity. Posteriorly, PPS in $Loxl1^{-/-}$ mice is stiffer and correlates with enlarged collagen fibril diameter, reduced elastin deposition, and irregular elastic fiber morphology. These findings together suggest that LOXL1 is integral to the structure and organization of scleral collagen and elastic fiber structures. LOXL1 deficiency could therefore influence the biological and biomechanical properties of ocular tissues which could contribute pathologically to XFG and related diseases.

Results

$Loxl1^{-/-}$ mice have increased anterior chamber depth, thinner central cornea, and reduced visual acuity

LOXL1 is highly expressed in the lens zonules, along with fibrillin-1, and may play a role in lens stability [39]. One of the hallmarks of ocular manifestations of XFS patients is phacodonesis due to weakened lens zonules [40]. To determine whether LOXL1 deficiency altered anterior eye morphology we investigated anterior chamber depth (ACD), central corneal thickness (CCT) and axial length (AL) using spectral domain optical coherence tomography (SD-OCT) in $Loxl1^{-/-}$ and Wt mice (Fig. 1). Representative OCT images of Wt and $Loxl1^{-/-}$ mice are shown in Fig. 1A and 1B, respectively. $Loxl1^{-/-}$ mice have a significantly deeper ACD compared with Wt (Fig. 1C; **p = 0.009,

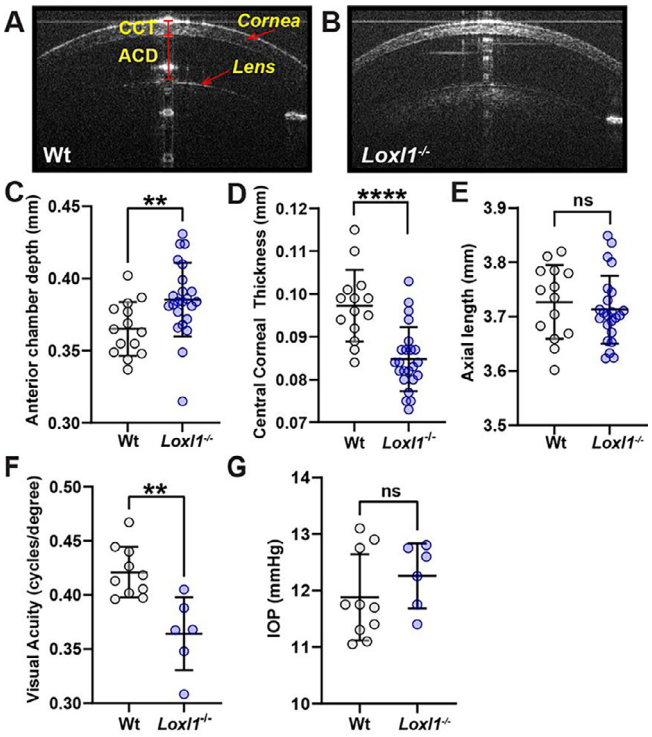

Fig. 1. *Loxl1*$^{-/-}$ mice have deeper ACD, thinner CCT and lower visual acuity without elevated intraocular pressure. Representative OCT images from (A) Wt and from (B) *Loxl1*$^{-/-}$ mice. ACD and CCT measurements are shown in A. (C) ACD is significantly increased in *Loxl1*$^{-/-}$ mice compared to Wt (n = 14 wt and n = 23 *Loxl1*$^{-/-}$; **p = 0.009). (D) CCT is significantly thinner in *Loxl1*$^{-/-}$ mice (n = 14 wt, n = 23 *Loxl1*$^{-/-}$; ****p < 0.0001). (E) AL was not significantly different between genotypes (n = 14 wt, n = 23 *Loxl1*$^{-/-}$; p = 0.537). (F) Optomotor response showed decreased visual acuity in *Loxl1*$^{-/-}$ mice compared with age-matched Wt mice (n = 10 wt, n = 6 *Loxl1*$^{-/-}$; **p = 0.007). (G) IOP was not significantly different between genotypes in mice at 12 months of age (n = 10 wt, n = 6 *Loxl1*$^{-/-}$; p = 0.280). Data presented as mean ± standard deviation. Statistical significance was evaluated by Welch's *t*-test.

Wt = 0.365 ± 0.019 mm vs *Loxl1*$^{-/-}$ = 0.385 ± 0.0 256 mm, n = 14 and 23, respectively). Some studies in humans have demonstrated thinner CCT in patients with XFS, regardless of XFG diagnosis [41]. To determine if lack of LOXL1 affected CCT in mice, we measured CCT using OCT in *Loxl1*$^{-/-}$ and Wt mice and found CCT was significantly thinner in *Loxl1*$^{-/-}$ mice (Fig. 1D; ****p < 0.0001, Wt = 0. 097 ± 0.008 mm vs *Loxl1*$^{-/-}$ = 0.085 ± 0.007 mm, n = 14 and 23, respectively). There was no significant difference in AL between Wt and *Loxl1*$^{-/-}$ mice (Fig. 1E; p = 0.537).

To assess visual acuity in mice, spatial acuity threshold was measured by optomotor response. *Loxl1*$^{-/-}$ mice experienced a 13.5 % decrease in visual acuity when compared to Wt mice (Fig. 1F, n = 10 wt and n = 6 *Loxl1*$^{-/-}$, **p = 0.006).

Loxl1$^{-/-}$ mice do not have increased IOP

Results from previous studies in *Loxl1*$^{-/-}$ mice are conflicting when IOP is considered; one study showed no elevation in IOP [42], while another showed increased IOP with age [43]. Factors such as background strain variation [44] and anesthesia [45,46] can significantly impact the outcome of IOP measurements. To reduce confounding variables in our study, we used littermate controls of identical genetic background and measured IOP in awake, behaving age-matched mice. Our results show that *Loxl1*$^{-/-}$ mice do not have elevated IOP compared to age-matched littermate Wt controls (Fig. 1G; n = 10 wt, n = 6 *Loxl1*$^{-/-}$; p = 0.280).

Optic nerve is enlarged in Loxl1$^{-/-}$ mice

We have previously shown a role for microfibrils in optic nerve expansion in microfibril deficient mice [47]. The optic nerve exits the eye posteriorly through the scleral opening. Because of the lack of collagenous LC in mice, the stability and elasticity of PPS are crucial in maintaining the function of optic nerve. *Loxl1*$^{-/-}$ mice recapitulate systemic features of XFS in humans, including pelvic organ prolapse due to weakening of the pelvic wall tissue [6,48,49], it is conceivable that *Loxl1*$^{-/-}$ mice experience optic nerve expansion due to impaired biomechanical property of PPS. To investigate whether lack of LOXL1 affects the scleral canal, we quantified optic nerve area in *Loxl1*$^{-/-}$ and Wt mice (Fig. 2). Representative optic nerve cross-sections show a noticeably enlarged optic nerve in

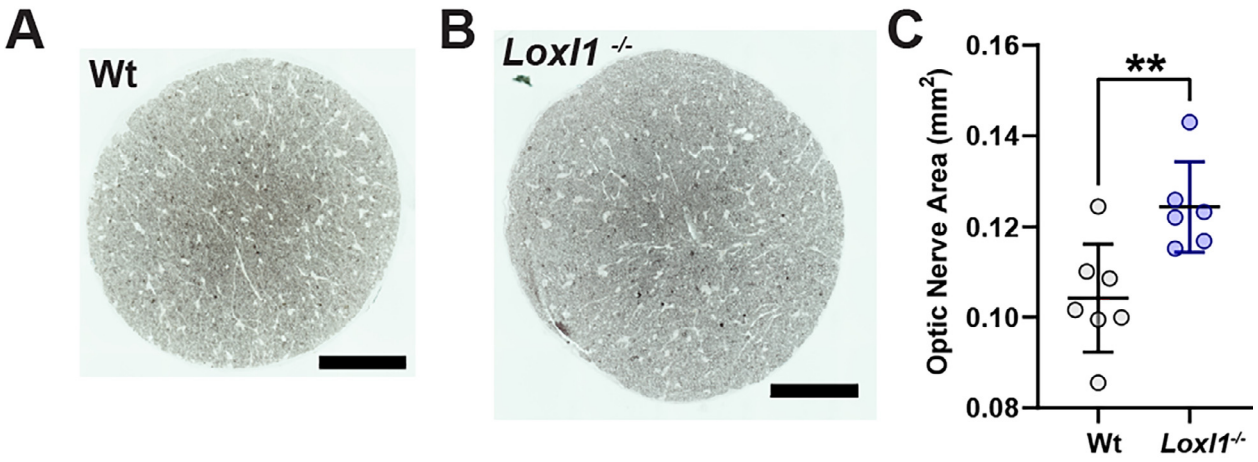

Fig. 2. Enlarged optic nerves in *Loxl1*$^{-/-}$ mice. Representative cross-sections of optic nerves from (A) Wt and (B) *Loxl1*$^{-/-}$ mice. (C) Optic nerve area measurements show enlarged nerves in *Loxl1*$^{-/-}$ mice (n = 7 wt, n = 6 *Loxl1*$^{-/-}$, ** p = 0.007; Welch's *t*-test). Scale bars = 100 μm.

Loxl1$^{-/-}$ mice (Fig. 2B) compared with Wt mice (Fig. 2A). Overall, optic nerve area was 19.3 % larger in *Loxl1*$^{-/-}$ mice compared with Wt (Fig. 2C; ** p = 0.007; Wt = 104241 ± 11953 μm^2 vs *Loxl1*$^{-/-}$ = 124362 ± 9989 μm^2, n = 7 and 6, respectively). These results suggest that lack of LOXL1 causes optic nerve expansion, possibly through alterations in the structural and biomechanical properties of the pia mater and PPS.

Elastic fiber morphology and density is altered in the PPS of Loxl1$^{-/-}$ mice

Previous studies in *Loxl1*$^{-/-}$ mice have identified abnormalities in elastic fiber morphology in the aorta [6] and in the trabecular meshwork [43]. Using TEM, we investigated elastic fiber morphology in the PPS. Elastic fibers in Wt mice have a densely stained elastin core, surrounded by microfibrils (Fig. 3A). In comparison, *Loxl1*$^{-/-}$ mice have a much less condensed elastin core (Fig. 3B; yellow arrowheads). The morphology of the elastin core in *Loxl1*$^{-/-}$ mice was notably irregular, and almost globular in structure (Fig. 3B; yellow arrowheads). Furthermore, *Loxl1*$^{-/-}$ mice also had elastic fiber with smaller cores surrounded by diffuse microfibrils (Fig. 3B; red arrowheads).

Next, we assessed the quantity of elastic fibers in the PPS. In *Loxl1*$^{-/-}$ mice the number of elastic fiber units present was noticeably less than in Wt animals. Fig. 4A, B show representative scleral strips of the PPS region 200–250 μm from the optic nerve head edge. Elastic fibers are highlighted by red circles and visually demonstrate the smaller number of elastic fiber units in *Loxl1*$^{-/-}$ mice. The number of elastic fiber units in each strip was manually quantified at a distance of 200–250 μm from the optic nerve head (Fig. 4C). We saw a significant 54 % decrease in the number of elastic units in *Loxl1*$^{-/-}$ mice compared with Wt animals (Fig. 4C; n = 8 samples from 4 animals for each genotype; **p = 0.0019). These data together suggest that lack of LOXL1 reduces elastin deposition and alters the morphology of elastic fibers in the PPS of mice.

Collagen fibrils in the PPS of Loxl1$^{-/-}$ mice are larger in diameter

LOXL1 plays an essential role in crosslinking elastic fibers[7] which is essential for strength and elasticity of tissue. However, the role of LOXL1 in collagen organization has not been well defined. Consistent with the importance of LOXL1 in elastic fiber function, *Loxl1*$^{-/-}$ mice develop pelvic floor organ prolapse due to malformation of elastic fibers [6,48]. We demonstrated *Loxl1*$^{-/-}$ mice exhibit changes in elastic fiber morphology in PPS, we next examined collagen fibril structure and organization. Representative electron micrographs of cross-sectional collagen in the PPS of Wt and *Loxl1*$^{-/-}$ mice are shown in Fig. 5A and 5B, respectively. Collagen fibrils in *Loxl1*$^{-/-}$ mice appeared larger in size, and with less defined borders. In Wt mice collagen fibrils have distinct edges, whereas *Loxl1*$^{-/-}$ mice frequently exhibit collagen fibrils with fissured edges. In *Loxl1*$^{-/-}$ mice, we also frequently observed apparent fusion of adjacent fibrils (Fig. 5B, orange arrowheads).

In addition to morphology, we measured the diameter of collagen fibrils in Wt and *Loxl1*$^{-/-}$ mice in the PPS. It is noteworthy that collagen fibrils that appeared fused with adjacent ones were more numerous in *Loxl1*$^{-/-}$ mice but were not included in this analysis due to ambiguity in distinguishing single collagen fibrils. To determine the range in diameters of collagen fibrils for each genotype, frequency histograms were plotted. In both genotypes, collagen fibrils in the PPS were not uniform in size, ranging from ~ 50 nm up to 225 nm (Fig. 5C). Collagen diameters showed a shift toward larger fibrils in *Loxl1*$^{-/-}$ mice

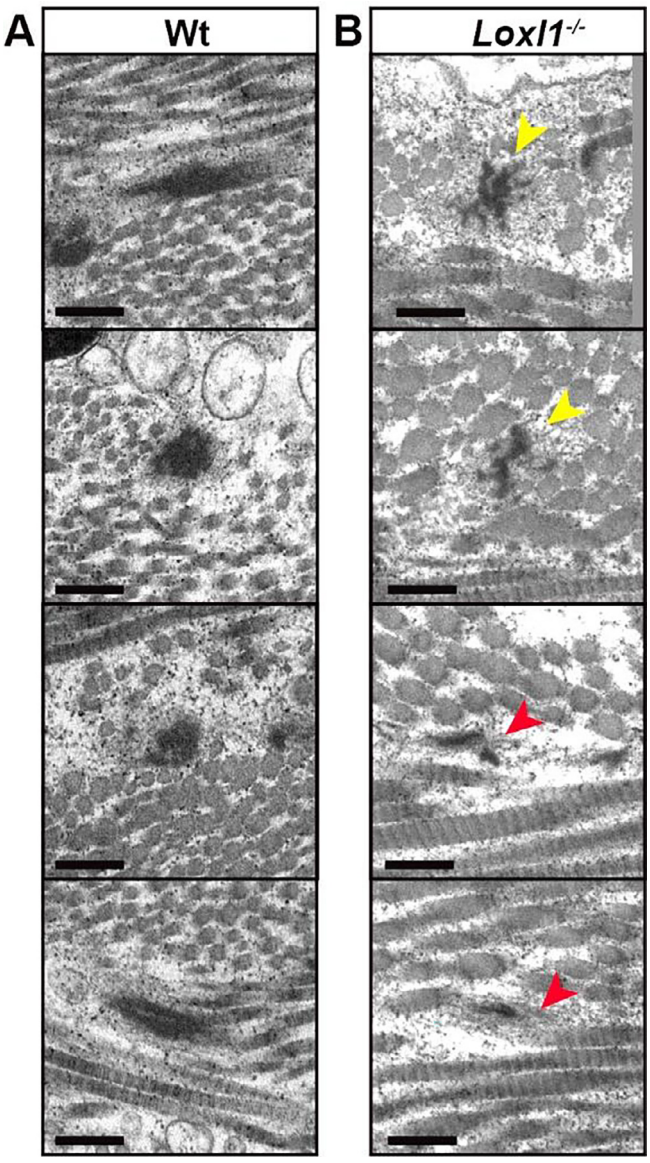

Fig. 3. Altered elastic fibers in the PPS of *Loxl1*$^{-/-}$ mice. Representative electron micrographs of the PPS of a (A) Wt and (B) *Loxl1*$^{-/-}$ mouse show tightly packed, densely stained elastin cores in Wt mice compared with altered elastin cores in *Loxl1*$^{-/-}$ mice. *Loxl1*$^{-/-}$ mice exhibit less dense, globular (yellow arrowheads) and smaller elastin cores (red arrowheads) surrounded by diffuse microfibril structures. Scale bars = 325 nm. (For interpretation of the references to colour in this figure legend, the reader is referred to the web version of this article.)

compared with Wt (Fig. 5C). To better visualize the range of data, violin plots showing the median along with upper and lower quartile values are shown in Fig. 5D. Wt mice have a collagen fibril size distribution that is generally smaller than *Loxl1*$^{-/-}$ mice (median = 98.86 nm vs 112.52 nm, upper quartile = 117.53 nm vs 128.72 nm, lower quartile = 84.53 nm vs 97.69 nm). The mean diameters of collagen fibrils were significantly increased by 10.5 % in *Loxl1*$^{-/-}$ mice compared with Wt mice (Fig. 5C; ****$p < 0.0001$, 102.5 ± 0.4 8 nm vs 113.3 ± 0.48 nm, n = 4 animals, 8 ROIs for each genotype). Our results suggest that lack of LOXL1 leads to larger collagen fibrils in the PPS.

To further examine the organization of collagen in PPS we assessed the density of collagen packing by calculating the nearest neighbor defined as the interfibrillar distance between collagen fibrils. To assess the range of interfibrillar distances, a frequency histogram was plotted. The nearest neighbor distance showed shift towards larger distances in *Loxl1*$^{-/-}$ mice compared with Wt (Fig. 5E). A violin plot shows the range in values of interfibrillar distances in Wt and *Loxl1*$^{-/-}$ mice (Fig. 5F; Wt median = 96.19 nm vs 101.5 nm, upper quartile = 114.2 nm vs 116.4 nm, lower quartile = 85.19 vs 88.85 nm; ****$p < 0.0001$). Mean nearest collagen neighbor distance was

significantly larger in *Loxl1*$^{-/-}$ compared with Wt mice (Wt = 101.1 ± 0.37 nm vs *Loxl1*$^{-/-}$ = 103.1 ± 0.30 nm; Wt n = 4, *Loxl1*$^{-/-}$ n = 4; ****p < 0.0001).

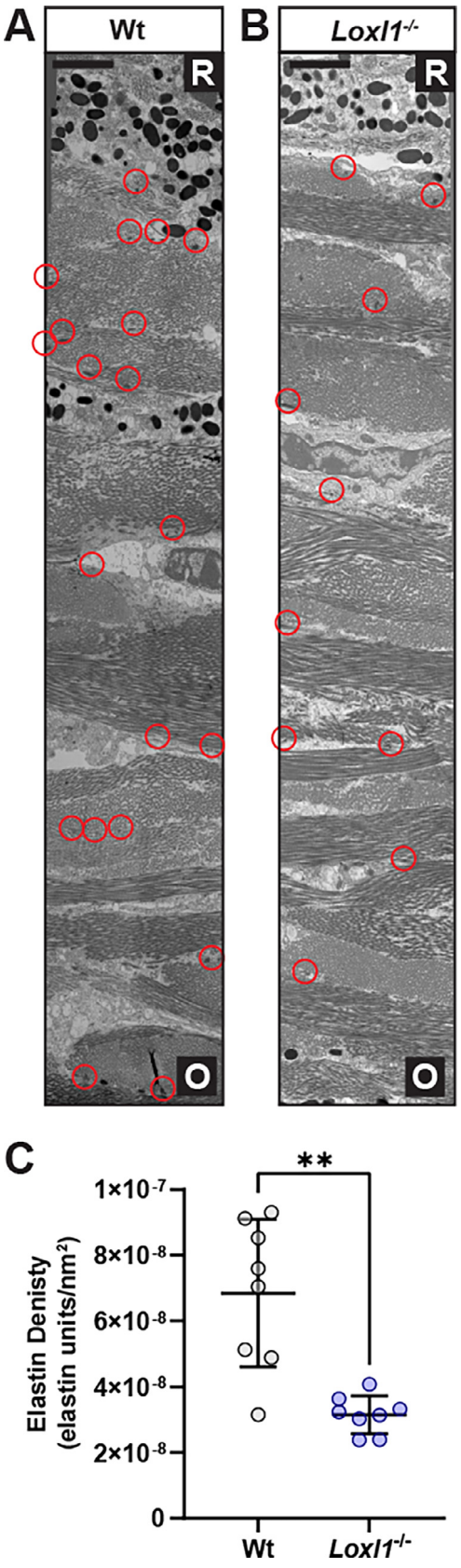

Qualitive and quantitative changes in collagen lamellae in the PPS of Loxl1$^{-/-}$ mice

Since the order and circumferential alignment of collagen lamellae can impact scleral thickness and tissue biomechanics [7,50,51], we compared collagen lamellae in the PPS of Wt and *Loxl1*$^{-/-}$ mice. In qualitatively assessing PPS strips, we observed that Wt mice had large bundles of collagen lamellae that appeared non-uniform in shape and thickness, indicating an irregular, interwoven structure [23] (Fig. 6A). In *Loxl1*$^{-/-}$ mice, however, collagen lamellae were smaller in size, forming thinner, more discreet layers that appeared more ordered than Wt mice (Fig. 6B). To further quantitate these findings, we analyzed the number of lamellae, lamellae thickness in scleral strips from Wt and *Loxl1*$^{-/-}$ mice. We found that the number of lamellae in *Loxl1*$^{-/-}$ mice was significantly increased when compared to Wt mice (Fig. 6C; Wt = 11.25 ± 2.66 vs *Loxl1*$^{-/-}$ = 18.60 ± 2.97; Wt n = 8 samples from n = 4 mice and *Loxl1*$^{-/-}$ n = 5 samples from 4 mice **p = 0.005). In addition to number of lamellae, the average lamellae thickness was measured. Lamellae thickness was significantly reduced in *Loxl1*$^{-/-}$ mice compared with Wt (Fig. 6D; Wt = 2695 ± 811.3 nm vs *Loxl1*$^{-/-}$ = 1804 ± 357.8 nm; Wt n = 8 samples from n = 4 mice and *Loxl1*$^{-/-}$ n = 5 samples from 4 mice *p = 0.019). The collagen arrangement in scleral tissue is interwoven such that collagen lamellae bundles are often differentially oriented, rather than organized in parallel to provide structural support to the tissue [23,52]. Together, these results suggest that in addition to collagen diameter changes, the arrangement of collagen lamellae is altered due to the lack of LOXL1.

PPS is stiffer in Loxl1$^{-/-}$ mice

The maturity of collagen and elastic fibers, and their mechanical properties are influenced by crosslinking that is partly mediated by LOXL1 activity [53]. We hypothesized that elastic fiber and/or collagen defects in *Loxl1*$^{-/-}$ mice may affect ocular tissue biomechanics. We applied AFM indentation on the PPS surface to measure the effect of the combined properties of scleral composition on tissue mechanics. Fresh sclera was flat-mounted and secured with a coverslip, exposing

Fig. 4. Elastic fiber reduction in the PPS of *Loxl1*$^{-/-}$ mice. Representative mosaic electron micrographs of a PPS strip from a (A) Wt and (B) *Loxl1*$^{-/-}$ mouse (resolution 2.4 nm/pixel; R = retinal side, O = outer scleral side). Red circles indicate location of elastin units. (C) Quantitation of elastin density in Wt and *Loxl1*$^{-/-}$ mice (n = 8 samples from 4 animals per group; **p = 0.0019; Mann-Whitney Test). Scale bars = 325 nm. (For interpretation of the references to colour in this figure legend, the reader is referred to the web version of this article.)

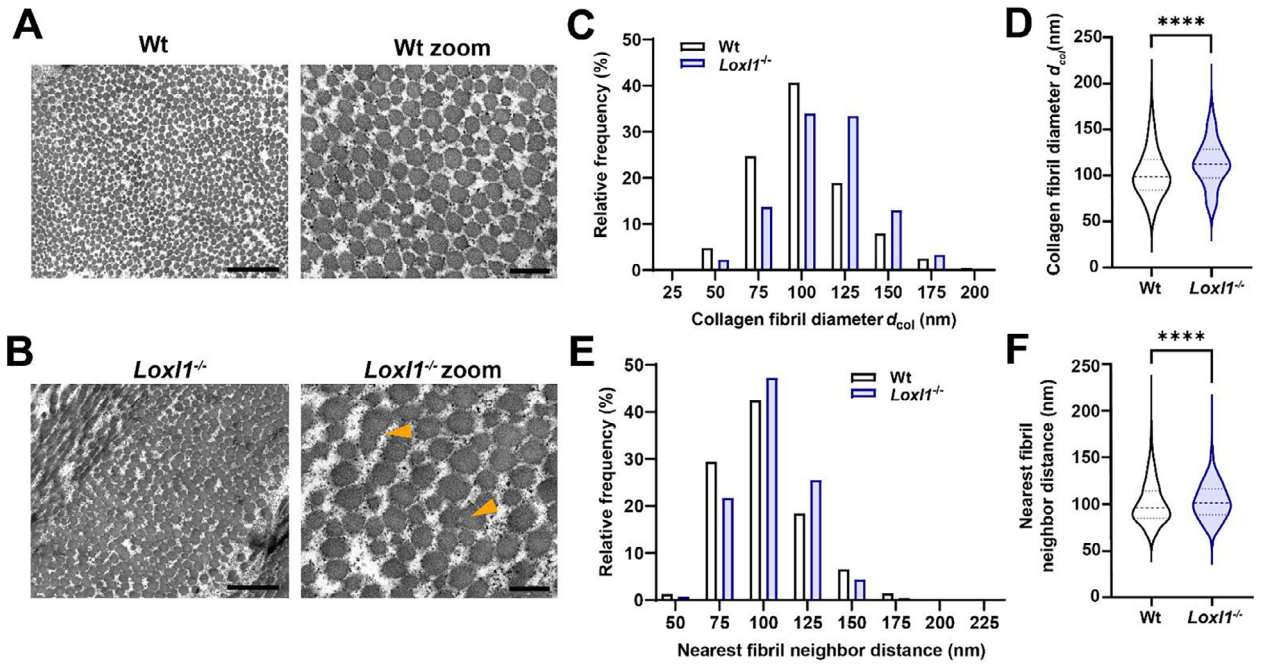

Fig. 5. Collagen fibrils are larger in the PPS of *Loxl1*$^{-/-}$ mice. Representative electron micrographs of (A) Wt and (B) *Loxl1*$^{-/-}$ collagen fibril cross sections in the PPS (scale bars = 800 nm for wide field, 200 nm for zoom) showing that the boundaries of collagen fibrils in *Loxl1*$^{-/-}$ mice are not as clearly defined as in Wt and appear fused with other fibrils (orange arrowheads). (C) Frequency distributions of collagen fibril diameters show a shift towards larger fibrils in *Loxl1*$^{-/-}$ mice (n = 3168 fibrils from 4 wt animals; n = 2884 fibrils from 4 *Loxl1*$^{-/-}$ animals). (D) Violin plots showing the median (dashed line) and upper/lower quartiles (dotted lines) for collagen fibril diameters (median = 98.86 nm Wt vs 112.5 nm *Loxl1*$^{-/-}$, upper quartile = 117.5 nm Wt vs 128.7 nm *Loxl1*$^{-/-}$, lower quartile = 84.53 nm Wt vs 97.69 nm *Loxl1*$^{-/-}$; ****p < 0.0001, Mann-Whitney test). (E) Frequency distributions of collagen fibril nearest neighbor distances in Wt and *Loxl1*$^{-/-}$ mice show a shift towards larger interfibrillar distances in *Loxl1*$^{-/-}$ mice (n = 3947 fibrils from 4 wt animals; n = 4532 fibrils from 4 *Loxl1*$^{-/-}$ animals, ****p < 0.0001). (F) Violin plots showing the median (dashed line) and upper/lower quartiles (dotted lines) for nearest neighbor distances (median = 96.19 nm Wt vs 101.5 nm *Loxl1*$^{-/-}$, upper quartile = 114.2 nm Wt vs 116.4 nm *Loxl1*$^{-/-}$, lower quartile = 85.19 nm Wt vs 88.85 nm *Loxl1*$^{-/-}$; ****p < 0.0001; Mann-Whitney test). (For interpretation of the references to colour in this figure legend, the reader is referred to the web version of this article.)

PPS tissue around the optic nerve head (Fig. 7A). Young's modulus of PPS within a 300 μm of the ONH region was measured by indentation onto the sclera (Fig. 7B). *Loxl1*$^{-/-}$ mice had significantly stiffer PPS than Wt mice (Fig. 7C; **** p < 0.0001; Wt = 2.636 ± 0.090 vs *Loxl1*$^{-/-}$ = 3.683 ± 0.128, n = 9 wt and n = 5 *Loxl1*$^{-/-}$; n_i = 306 and 221 indents, respectively). To examine the distribution of Young's modulus values obtained, a frequency histogram was plotted (Fig. 7D). The predominant values for Young's modulus obtained for Wt mice were between 1 and 1.5 kPa (Fig. 7D; arrow 1). *Loxl1*$^{-/-}$ mice, however showed a larger distribution in Young's modulus values, with a higher frequency of values between 4 and 4.5 kPa than Wt (Fig. 7D; arrows 2 and 3). In addition, higher values exceeding 7 kPa were only obtained for *Loxl1*$^{-/-}$mice (Fig. 7D; arrow 4). Our results indicate that LOXL1 deficiency leads to increased PPS stiffness in mice.

Discussion

The work described herein improves our understanding of how LOXL1 influences the ultrastructural organization of the ECM in PPS that correlates with changes in scleral tissue biomechanics. We found that *Loxl1*$^{-/-}$ mice experience no significant change in IOP at advanced age. IOP is determined by the balance between the rate of aqueous humor production and the rate of its outflow through the trabecular meshwork and uveal scleral pathways [54]. Proper functioning of the outflow pathways in the eye enables IOP to be maintained within a relatively narrow range [55]. The resistance of the trabecular meshwork outflow pathway which is the major regulator of IOP is partially governed by the tissue that is rich in collagen and elastic fibers [56]. Conflicting results on the impact of the absence of LOXL1 on

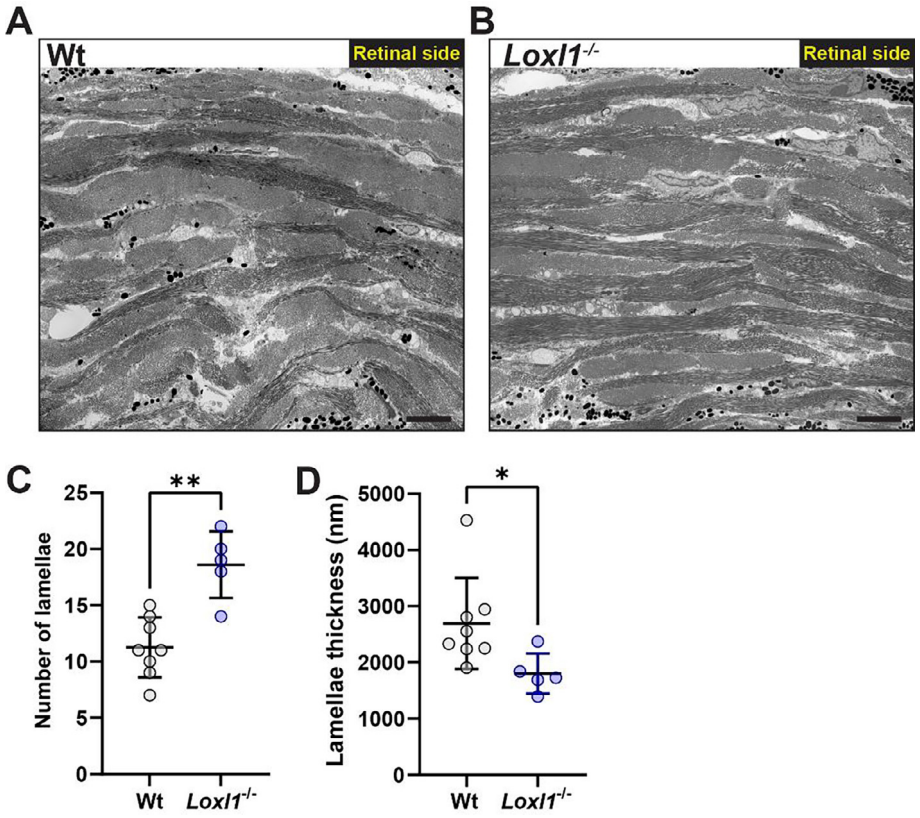

Fig. 6. Collagen lamellae in PPS of Wt and *Loxl1*$^{-/-}$ mice. Representative electron micrographs of PPS from a (A) Wt mouse and (B) *Loxl1*$^{-/-}$ mouse. Wt mice have larger lamellae layers compared to collagen lamellae in a *Loxl1*$^{-/-}$ mice which appear thinner and more striated. Scale bars = 5 μm. (C) Quantification of lamella layers in Wt and *Loxl1*$^{-/-}$ mice indicate that *Loxl1*$^{-/-}$ mice have increased numbers of collagen lamella (n = 8 samples from n = 4 mice Wt and n = 5 samples from 4 mice *Loxl1*$^{-/-}$, **p = 0.005; Mann-Whitney test). (D) Lamellae thickness is decreased in *Loxl1*$^{-/-}$ mice compared to Wt (n = 8 samples from n = 4 mice Wt and n = 5 samples from 4 mice *Loxl1*$^{-/-}$, *p = 0.0019; Mann-Whitney test).

IOP have been reported in studies using the *Loxl1*$^{-/-}$ mouse model. In one study, no elevations in IOP were observed with increasing age [42]. However, the strain used was different and controls were not littermates, which could impact IOP readings [44,46]. In another study, IOP was reported to be increased in *Loxl1*$^{-/-}$ mice accompanied with a paradoxical reduction in trabecular meshwork outflow resistance, however strain background differences may be a confounding factor in this study as well [43]. IOP measurements in mice can be highly variable due to differences in anesthesia [45,57] and genetic background [44,46]. Our results in non-anesthetized *Loxl1*$^{-/-}$ mice showed no elevations in IOP compared to littermate Wt mice at 1 year of age (Fig. 1G). These findings suggest that lack of LOXL1 does not alter IOP in mice.

We report that *Loxl1*$^{-/-}$ mice exhibit deeper ACD, thinner CCT but no change in AL (Fig. 1). In humans, XFS has a high prevalence of dislocated lens phenotypes due to zonule abnormalities [58]. The biometric changes that we observed in *Loxl1*$^{-/-}$ mice, including deepening of the anterior chamber in the absence of axial length alteration, are possibly due to weakening of the zonules resulting in lens dislocation posteriorly to the vitreous cavity. Lens zonules are composed of elastin-free fibrillin microfibril bundles and recent studies have found that in addition to fibrillin-1 being the most abundant protein, LOXL1 is also highly expressed in the zonules [39,59]. Although the best-known function of LOXL1 is crosslinking tropoelastin to elastin, and elastin is distinctly absent in the lens zonules [39,60], our biometric findings that are indictive of lens dislocation in *Loxl1*$^{-/-}$ mice suggests a possible role of LOXL1 in zonule formation. The lens dislocations also most likely explain the decreased visual acuity in *Loxl1*$^{-/-}$ mice as a result of the inability to focus images correctly on the retina. In addition, although we did not observe any gross lens abnormalities on slit lamp examination (data not shown), lens abnormalities have been reported in *Loxl1*$^{-/-}$ mice, including lens fiber changes consistent with cataract formation [42], which could also contribute to the decreased visual acuity observed in this study.

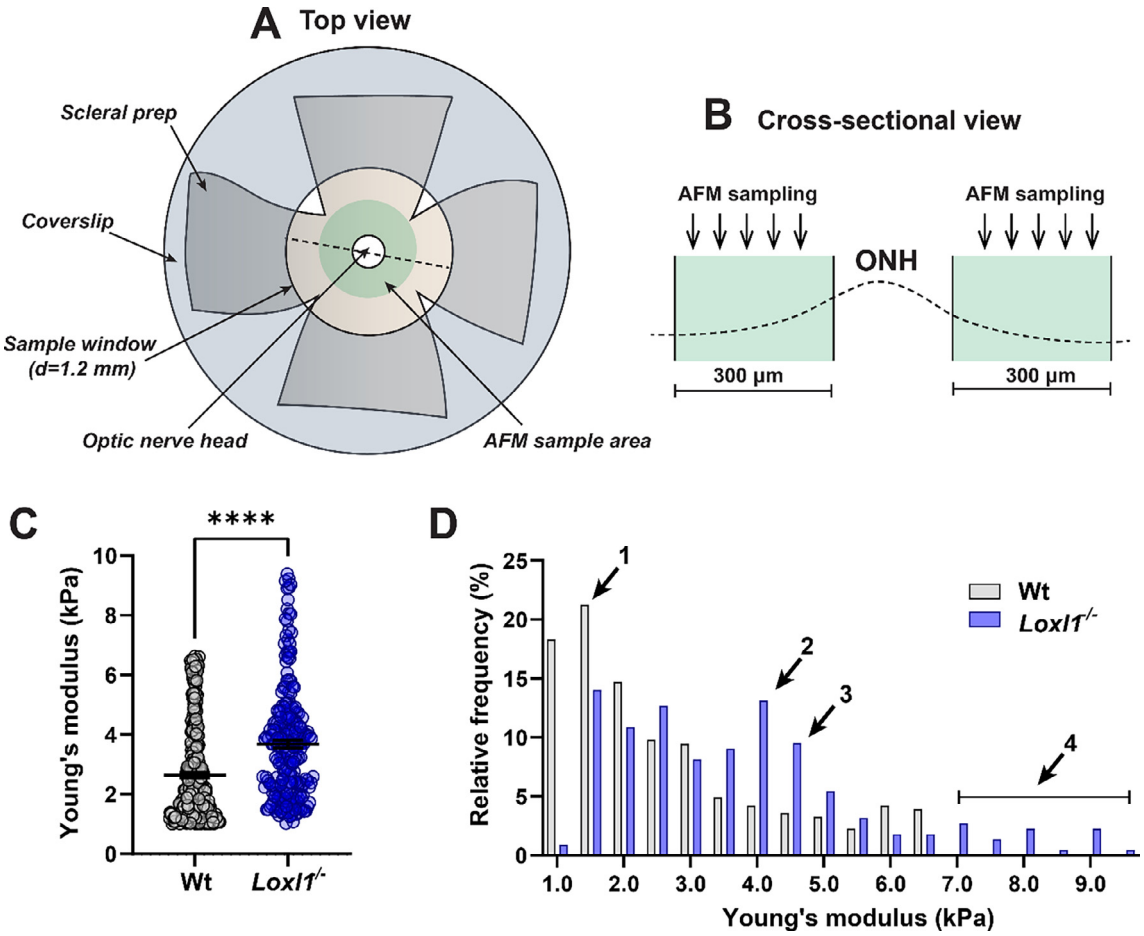

Fig. 7. PPS is stiffer in *Loxl1*$^{-/-}$ mice. (A) Top view (scleral side up) of the scleral preparation for AFM. A 13 mm Thermanox coverslip was modified using a biopsy punch to allow for a tissue access window (diameter = 1.2 mm). The 300 μm AFM sample area is indicated as the green radial zone around the optic nerve head. (B) Cross sectional view of the scleral prep (dashed line) with 300 μm peripapillary sample zones indicated in green with direction of AFM indents (taps) indicated by arrows. (C) Young's modulus measurements of Wt (n = 9 animals, n_i = 306 indents) and *Loxl1*$^{-/-}$ (n = 6 animals, n_i = 221 indents) mice show differences in stiffness of the PPS between genotypes (****p < 0.0001; Mann-Whitney test, data plotted as mean ± S.E.M. (D) Frequency histogram showing relative frequency of Young's modulus values for Wt and *Loxl1*$^{-/-}$ mice; arrows 1–4 highlight values most different between genotypes. n = number of animals, n_i = number of AFM indents. (For interpretation of the references to colour in this figure legend, the reader is referred to the web version of this article.)

Interestingly, we found that *Loxl1*$^{-/-}$ mice had enlarged optic nerves compared with Wt mice (Fig. 2). The optic nerve is ensheathed by the pia mater which is rich in elastic fibers and expansion of the optic nerve canal is indicative of a change in biomechanical properties of the tissue. We previously reported that mice with a heterozygous mutation in the *Tsk* gene (*Fbn1*$^{Tsk/+}$) had abnormal microfibrils and increased nerve area [47]. In that study, we focused on microfibrils because of the *fbn-1* mutation and reported thinning of the pia mater in those *Fbn1*$^{Tsk/+}$ mice. Although fibrillin microfibrils are pre-requisite for elastic fiber formation, LOXL1 is required for elastin core formation as well. *Loxl1*$^{-/-}$ mice have been shown to have enlarged episcleral veins and Schlemm's canal [43], possibly due to the breakdown of elastic fibers and decreased structural integrity of vessel tissues. Similarly, our observation of enlarged optic nerves also suggests reduced structural integrity of the pia mater which plays a role in the structure and stability of the optic nerve [61,62].

Previous work in humans [33,63], non-human primates [33], and mice [64,65] have well documented the elastic fiber arrangement in the sclera. In mice and humans, elastic fibers are found circumferentially in the peripapillary region surrounding the ONH, decreasing in concentration towards the limbus [33,65]. Elastic fibers in *Loxl1*$^{-/-}$ mice were amorphous and smaller in shape, lacking dense elastin cores compared to Wt mice (Fig. 3). We also found that elastic fiber content was significantly reduced in the PPS of *Loxl1*$^{-/-}$ mice (Fig. 4). These results together suggest that LOXL1 is crucial for

elastic fiber structure and deposition in the PPS. Our findings are consistent with previous reports; reduced elastic fibers and disorganized elastin core morphology has also been reported in the thoracic aorta and dermis of *Loxl1*$^{-/-}$ mice [6]. Furthermore, knockdown of LOXL1 expression reduced elastin crosslinking and subsequent elastic fiber deposition in a mouse model of liver fibrosis [66]. LOXL1-driven elastic fiber phenotypes have also been observed *in vitro*; vaginal wall cells derived from *Loxl1*$^{-/-}$ mice have decreased elastic fiber production [67]. The reduced elastic fiber content and aberrant morphology in the PPS of *Loxl1*$^{-/-}$ mice may have implications for tissue stiffness and biomechanics, as discussed below.

Many previous LOXL1 studies have shown reduced crosslinking and aberrant formation of elastic fibers, so it was therefore not surprising to discover significant reduction and morphological changes of elastic fibers in the PPS of *Loxl1*$^{-/-}$ mice. However, the role of LOXL1 in collagen formation is less defined. Interestingly our work demonstrates that absence of LOXL1 results in significant changes to scleral collagen structure and organization. In the human PPS, collagen fibrils are not uniform in size, and can vary throughout the depth of the sclera, assembling into interwoven lamellae that give rise to increased tensile strength [32,33,68]. Since LOXL1 has been implicated in the crosslinking of collagen[2], we investigated whether *Loxl1*$^{-/-}$ mice had differences in collagen morphology in the PPS. We discovered a role for LOXL1 in regulating collagen fibril diameter and fibril packing density. Collagen fibrils in the PPS of *Loxl1*$^{-/-}$ mice were enlarged and highly amorphous, with incidences of adjacent fibrils appearing to fuse together (Fig. 5B). The apparent difference in fibril size between Wt and *Loxl1*$^{-/-}$ is striking and reached statistical significance. However, it is important to note that we did not include fused collagen fibrils, which are more prominent in *Loxl1*$^{-/-}$ mice, in our analysis of fibril diameter. Our data is therefore potentially underestimating the observed increase in fibril diameter in *Loxl1*$^{-/-}$ mice. Increased fibril diameter coincided with increased interfibrillar spacing, which is most likely driven by the increase in fibril diameter itself. Interestingly, a similar effect of the absence of LOXL1 on collagen morphology has been reported in other tissues. In bone collagen, reduced LOXL1 expression was correlated with an increase in irregularly shaped fibrils [69]. In a study using β-aminoproprionitrile (BAPN), an irreversible pan-LOX inhibitor, collagen fibrils became irregular in structure and multiple adjacent fibrils appeared fused [70]. Additionally, in an *in vitro* study BAPN altered the structure and regularity of collagen molecules [71]. Similarly, our results indicate that LOXL1 plays a key role in formation of scleral collagen fibrils *in vivo* in the PPS. Collagen formation *in vivo* is a complex process that is not yet fully understood [72]. Although TEM offers high resolution imaging of tissue structures, the method relies on fixation and processing of tissue. Additional methods such as AFM and cryo-EM which better maintain the native state of the tissue may shed more light on the structural differences we observe in *Loxl1*$^{-/-}$ mice. Nevertheless, our results reinforce collagen phenotypes seen in other studies of LOXL1 deficiency and implicate a potential role of LOXL1 on collagen diameter and organization that warrants further investigation.

In addition to increased collagen fibril diameter in *Loxl1*$^{-/-}$ mice, we observed differences in collagen lamellae organization (Fig. 6). The layers of collagen lamellae in Wt mice were generally thicker and non-uniform in size, with interweaving between layers (Fig. 6A). In *Loxl1*$^{-/-}$ mice however, we observed thinner, orderly, more uniformly sized layers of collagen lamellae with less waviness and interweaving (Fig. 6B), suggesting deviation from the usually interwoven layers of collagen observed in the PPS [23]. Upon quantitation we observed that collagen lamellae in *Loxl1*$^{-/-}$ mice were both increased in number and were on average thinner than lamellae in Wt mice (Fig. 6C, D). Collagen lamellae in the PPS are typically interwoven for strength and appear wavy at low load [73] and progressively straighten under external load, which causes lamellae to exhibit strain-stiffening behavior [74]. Circumferential organization of collagen lamellae in the PPS is also essential for ONH biomechanics [23]. In human myopia, changes in posterior collagen fiber alignment in the PPS from circumferential to a more radial alignment occur, affecting tissue biomechanics [50]. Our structural observations may in part explain the biomechanical changes in the PPS tissue as discussed below. Investigating the impact of LOXL1 on collagen interweaving and collagen post-translational modifications will be crucial to further understand the impact of LOXL1 on scleral organization and stiffness.

The changes in elastic fiber and collagen composition and structure that we have observed in *Loxl1*$^{-/-}$ mice can impact the stiffness and viscoelastic properties of tissue [75]. We applied AFM indentation on the PPS surface to measure the effect of the combined properties of scleral composition on tissue mechanics. We found that PPS is significantly stiffer in *Loxl1*$^{-/-}$ mice (Fig. 7). Working together with collagen, elastic fibers are important for tissue compliance, i.e., the ability of a tissue's structure to deform under a given load, and are the primary driving force of elastic tissue recoil after a deformative force has been released [75]. Increasing the elastic fiber-to-collagen ratio leads to a decrease in tissue stiffness [76], whereas a decrease in elastic fiber content has the opposite effect [75,77]. Consistent with this notion, our findings show that decreased elastic fiber in the PPS in *Loxl1*$^{-/-}$ mice leads to increased stiffness. Interestingly, changes in collagen diameter have been

noted in patients with pelvic organ prolapse; pelvic floor connective tissue had larger, stiffer collagen fibrils in a loosened arrangement which weakened load-bearing capacity [78]. We identified an increase in tissue stiffness at the macroscale, however, many ECM factors need to be taken into account when considering mechanical properties of tissue including the individual stiffness of tissue components themselves at the microscale, such as individual collagen fibril stiffness, density, and organization [75].

The finding that *Loxl1*$^{-/-}$ mice have a significantly stiffer PPS has implications in terms of eye diseases. XFS is a significant risk factor for XFG [21,22,17]. Major risk factors associated with glaucoma are increasing age and sensitivity to IOP elevation and fluctuation [26]. Increasing age increases the stiffness of scleral tissue [79–81], possibly due to increased collagen crosslinking [82,83]. Such changes in scleral stiffness alter the biomechanics of the ONH [84], which likely impact the susceptibility of RGC axons to elevated IOP. While exiting the ONH, RGC axons are subjected to translaminar pressure influenced by IOP and tissue pressure. The hoop stress regulated by PPS biomechanical property is also important in maintaining normal axon function.

Stiffness of the PPS in XFG has been measured in human samples, revealing a decrease in stiffness of tissue in XFG patients, with a caveat that the results were from single AFM indentations and therefore not statistically significant [85]. Our data is robust in demonstrating a role for LOXL1 in scleral structure and biomechanics; however, we also recognize that indentation with AFM in tissue that is subjected to highly dynamic physiological and pathological changes has significant limitations, especially in light of glaucoma pathogenesis. Inflation testing is technically challenging but may be needed to confirm our findings. Lastly, it is worth noting that many studies have revealed an association between myopia and glaucoma. The likely mechanistic explanation for such an association between these two clinical entities is their shared common feature - defective ocular biomechanics [3]. Not surprisingly, exploiting collagen crosslinking in the sclera to halt the disease progression has been investigated as a potential treatment of both myopia and glaucoma [86–88]. Further understanding the role of LOXL1 in the ultrastructure and stability of the PPS may illuminate underlying pathological mechanisms in XFG and other ocular diseases where understanding the biomechanical properties of tissue are paramount.

Taken together, our results indicate that LOXL1 has a fundamental role in the ultrastructure of collagen and elastic fiber and consequently in the biomechanical properties of the PPS in mice. Lack of LOXL1 reduced elastic fiber content of the PPS, but also significantly altered the ultrastructure of collagen fibrils. LOXL1-dependent changes in the ultrastructure of the PPS coincided with increased stiffness of the PPS and enlargement of the optic nerve. Our findings highlight LOXL1 as integral to the biomechanical properties of the PPS which may further our understanding of ocular disease.

Experimental procedures

Animals

All experiments were carried out in accordance with the Association for Research in Vision and Ophthalmology (ARVO) statement for the Use of Animals in Ophthalmic and Vision Research and were approved by the Vanderbilt University Institutional Animal Care and Use Committee. We obtained *Loxl1*$^{-/-}$ mice on a 129S background from Dr. Tiansen Li [6]. Wild type (Wt) 129S littermates were used as controls. Equal numbers of male and female mice aged between 49 and 52 weeks were used for all experiments in this study. Mice were housed in a facility managed by Vanderbilt University Division of Animal Care, with *ad libidum* access to water and standard mouse chow and a 12 h light cycle (lights on at 6:30 a.m. and off at 6:30p.m.).

Confirmation of genotype by polymerase chain reaction

Tail clipping was performed between 3 and 6 weeks of age under isoflurane anesthesia. DNA extraction was performed using a DNeasy Mini Kit (Qiagen, Valencia, CA) according to the manufacturer's instructions. The following primers were used: S32 5′- ACA CGT CGG TGC TGG GAT CA-3′; D5 5′-CTT TCGTAA ACC AGT ATG AGA ACT ACG ATC-3′; and N5 5′-CGA GAT CAG CCT CTG TTC CAC-3′ (IDT, Coralville, IA) [6]. Genotyping was performed to identify *Loxl1*$^{+/+}$ and *Loxl1*$^{-/-}$ mice using primers designed to amplify a region in exon 1 of the wild type *Loxl1* gene (~400 bp product) and the inserted mutant Neo cassette (~310 bp product). The Neo cassette insertion introduces a translation stop codon in exon 1 of the *Loxl1* transcript.

IOP measurements

IOPs were measured in awake, behaving mice at the same time of day (between 1 and 3 PM). To prepare for awake, behaving measurements, mice were handled daily for 6 days prior to IOP measurement. Briefly, on days 1–4 prior to measurement mice were scruffed and held in a position analogous to the position used for actual IOP measurement, held for 30 s and then released. On days 5–6 mice were handled and scruffed in the same manner but with the addition of topical anesthesia (0.5 % proparacaine

hydrochloride; Akorn Inc, Lake Forest, IL) and a TonoLab rebound tonometer (iCare, Franconia, NH) held near the eye without actual measurement. IOPs were then acquired on day 7 after application of the same topical anesthesia. Ten TonoLab final readings each were averaged to obtain a single IOP value per eye.

SD-Oct

OCT was carried out as previously described [89]. Mice were anesthetized with ketamine (100 mg/kg) and xylazine (7 mg/kg) in saline. One eye from each mouse was visualized using the Bioptigen Envisu R2200 SD-OCT system (Leica Microsystems, Wetzlar, Germany). A 12-mm telecentric bore lens was used along with a rectangular scanning pattern consisting of 100B-scans, each composed of 1000 A-scans. The ACD was defined as the distance from the inner surface of the central cornea to the central anterior surface of the lens. Both CCT and ACD were determined by the digital caliper function of the Diver Analysis Software (Leica Microsystems). For AL measurements, pupils were dilated using 1 % tropicamide (Bausch & Lomb, Laval, QC, Canada) and imaging was performed using a "mouse retina" lens (Leica Microsystems). AL was determined by the acquisition of a series of three images. 1) A posterior image was used to determine the distance from the outer retinal pigment epithelium to the posterior surface of the lens (vitreous + retina); 2) an anterior image was used to determine the distance from the outer corneal surface to the anterior surface of the lens ([CCT] + ACD); and 3) an image in which the lens was optically folded in half to determine half of the axial lens diameter (1/2 lens). AL was defined as equal to (vitreous + retina) + (CCT + ACD) + 2 $\times$ 1/2 lens. Upon completion of imaging, the mice were injected with atipamezole (1 mg/kg; Patterson Veterinary, Greeley, CO, USA) to reverse anesthesia and to prevent xylazine-induced corneal damage [90].

Optomotor response test

Photopic visual acuity of mice was assessed by the optomotor response. Mice were placed, unrestrained, on an elevated platform centered among four adjoining LCD screens (OptoMotry; Cerebral Mechanics Inc., Canada). Spatial frequency thresholds were measured by assessing the oculomotor response to drifting sinusoidal gratings at 100 % contrast. Grating spatial frequency (cycles/degree) was systematically adjusted based on the optomotor response noted by a naïve experimenter. Mice were tested at least twice to determine baseline spatial acuity.

Optic nerve evaluation

Mice were euthanized and eyes were rapidly enucleated, and optic nerves cut approximately 1.5 mm from the globe and post-fixed in 4 % paraformaldehyde in phosphate-buffered saline (PBS). Optic nerves were transferred to 2 % osmium tetroxide in PBS for 1 h before dehydration and embedding in Epon-812/Araldite resin, as previously described [47]. Using an ultramicrotome (Leica EM UC7, Wetzlar, Germany), 1-μm-thick cross-sections of optic nerves were cut, stained with paraphenylenediamine (PPD), which darkly stains axoplasm of degenerating axons in light microscopy,[91] and mounted with Permount Mounting Medium (Thermo Fisher Scientific, Waltham, MA, USA). Stained optic nerve cross-sections were imaged with an oil immersion 100X objective on a Nikon inverted light microscope equipped with an SLR DS-Ri2 camera (Nikon, Melville, NY, USA). Montage images covering the entire nerve cross-section were taken using the NIS-elements software (Nikon). Optic nerve area, excluding the pia mater, was determined by drawing a polygon around the nerve using ImageJ.

Tem

Immediately after euthanasia, eyes were rapidly enucleated and placed into cold 1x PBS on ice. Scleral samples were obtained by immediate dissection of the eye. Briefly, eyes were bisected posterior to the equator and cornea was removed, followed by the lens and retina. Using a biopsy punch and optic nerve head as a central marker, 1.5 mm PPS samples were obtained and immediately placed into 2.5 % glutaraldehyde in 1x PBS for 1 h rotating at room temperature. Samples were postfixed sequentially in 1 % tannic acid, 1 % OsO4, and en-block stained with 1 % uranyl acetate. The samples were dehydrated in a graded ethanol series and infiltrated with EMbed-812 resin (Electron Microscopy Sciences, Hatfield, PA, USA) using propylene oxide as the transition solvent. The resin was polymerized at 60 °C for 48 h. Thick sections were cut at a nominal thickness of 500 nm and stained with toluidine blue to locate the center of the sclera. Thin sections were taken at a nominal thickness of 70 nm and collected on 200 mesh Ni grids. All grids were stained with 1 % phosphotungstic acid to increase collagen and elastin contrast followed by 1 % UA and lead citrate. Imaging was carried out using a Tecnai T12 operating at 100 kV equipped with an AMT nanosprint CMOS camera using SerialEM acquisition software. Zones of interest analogous to AFM (see below) measurements were identified between 200 and 250 μm by measuring the distance from the edge of the optic nerve. At this distance, a tiled image

strip with a nominal width of 6.6 μm was taken through the entire depth of the peripapillary sclera, these images were assembled and blended using the IMOD software suite.

Analysis of EM images for collagen and elastic fibers

Analysis to determine the diameter of collagen fibrils and to find the center of each fibril was carried out using ImageJ followed by nearest neighbor analysis using Matlab. Briefly, for each strip image, two 2.4 μm^2 regions of interest (ROI) containing round, cross-sectional collagen fibrils were identified at approximate distances of 40–60 μm and 80–100 μm from choroid layer by a masked observer. Collagen fibril area was measured for all individual fibrils within the ROI using ImageJ and fibril diameter calculated as equal to 2 times the square root of the area/pi. Nearest neighbor analysis was performed similar to a previously described method [92]. Briefly, X/Y coordinates of the center of individual collagen fibril cross-sections were mapped using ImageJ [93] and imported into Matlab. For each fibril, coordinate vectors to all local fibrils were determined and the magnitude of the shortest vector at each fibril defined the nearest neighbor distance. For elastic fiber unit quantification, masked observers manually counted elastic fiber units within each strip. For normalization, the number of elastic fiber units were divided by total strip area as measured using ImageJ. After analysis, masked observers were unblinded and data plotted.

Analysis of EM images for collagen lamella

Analysis to determine the number and thickness of collagen lamellae was carried out using ImageJ software. For each image strip, a fixed line measuring 40 μm was placed along the center of the image. The number of collagen lamellae along the line were counted and measurements of lamellae thickness were taken manually using ImageJ.

Sample preparation for AFM

Scleral samples were obtained in the same fashion as for TEM. Briefly, eyes were bisected posterior to the equator. Cornea was removed, followed by the lens and retina. For scleral flat mount, samples were cut and prepared in a four-leafed display. Sclera samples were mounted in a custom-made soft-clamping immobilizing retainer of tissue (SCIRT) dish prepared using a published protocol [94] (see Supplemental Fig. 1). In brief, sclera samples were placed scleral side up on a polydimethylsiloxane (PDMS)-coated petri dish (50 mm diameter, Corning, NY). Using 36 mm diameter plastic cover slips with a central window of 1.2 mm diameter (Thermanox, Rochester, NY) and superglue (Loctite gel control, Henkel Corporation, CT), samples were secured and 1x PBS placed on sample to maintain hydration. AFM was preformed within 1 h of harvesting samples.

Elastic modulus measurement with AFM

Young's modulus was measured using AFM in contact mode force (AFM; MFP-3D, Asylum Research, CA). Indentations were performed in the PPS up to 300 μm from the edge of the optic nerve head. Force-displacement curves were taken at 20 points within each region, for a total of 40–60 indentations for each eye. Under single force mode, indentations were made at a loading rate of 2 μm/s and trigger force of 5 nN with silicon nitride cantilevers with a nominal spring constant of 0.06 N/m and a 5 μm diameter spherical polystyrene bead (Novascan, Boone, IA). The AFM tips were calibrated before use and had an average spring constant of 80 ± 20 pN/nm. Force-displacement curves were fit to the Hertz model assuming a Poisson's ratio of 0.45 using the Asylum curve fitting software to determine the elastic modulus.

Statistical analysis.

All experiments were carried out by masked observers. All data are presented as mean ± standard deviation (SD) unless otherwise stated. Graphs were made and statistical analyses were performed using GraphPad Prism version 9.0 (GraphPad Software, San Diego, CA). Data were analyzed using Student's two-tailed *t*-test as indicated in the figure legends. For larger datasets, we first determined if the data were normally distributed using a Shapiro-Wilk test of normality. In cases where data were normally distributed, we performed parametric statistics, e.g., *t*-tests. Where data was not normally distributed, we carried out non-parametric tests, e.g., Mann-Whitney test, as indicated in figure legends. We defined statistical significance as $P \leq 0.05$. Number of measurements and specific P-values are indicated in results or figure legends.

Author contributions

RWK and JK conceived the study. RWK, JK, LKW and HJW designed the experiments and LKW, HJW, EK, and YW performed the experiments. LKW, RWK, and JK wrote the manuscript. CRK and EK provided critical comments during manuscript preparation.

Funding sources

The work carried out in this manuscript was funded by Nation Institute of Health (NIH) grants awarded to RWK (R01EY020894) and the Shaffer Award from Glaucoma Research Foundation to RWK. This work was also supported by a

departmental unrestricted award by Research to Prevent Blindness, Inc. Imaging was supported through the Vanderbilt University Medical Center Cell Imaging Shared Resource core facility and NIH grant DK020593. Electron microscopy was performed in part through the use of the Vanderbilt Cell Imaging Shared Resource (supported by NIH grants CA68485, DK20593, DK58404, DK59637 and EY08126).

DECLARATION OF COMPETING INTEREST

The authors declare that they have no known competing financial interests or personal relationships that could have appeared to influence the work reported in this paper.

Appendix A. Supplementary data

Supplementary data to this article can be found online at https://doi.org/10.1016/j.mbplus.2022.100120.

Received 4 August 2022;
Accepted 17 August 2022;
Available online 21 August 2022

Keywords:
Lysyl oxidase-like 1;
Exfoliation glaucoma;
Peripapillary sclera;
Extracellular matrix;
Transmission electron microscopy;
Atomic force microscopy

References

[1]. Csiszar, K., (2001). Lysyl oxidases: a novel multifunctional amine oxidase family. *Prog. Nucleic Acid Res. Mol. Biol.*, **70**, 1–32.
[2]. Greene, A.G., Eivers, S.B., Dervan, E.W.J., O'Brien, C.J., Wallace, D.M., (2020). Lysyl Oxidase Like 1: Biological roles and regulation. *Exp. Eye Res.*, **193**, 107975
[3]. Vallet, S.D., Ricard-Blum, S., (2019). Lysyl oxidases: from enzyme activity to extracellular matrix cross-links. *Essays Biochem.*, **63**, 349–364.
[4]. Thomassin, L., Werneck, C.C., Broekelmann, T.J., Gleyzal, C., Hornstra, I.K., Mecham, R.P., Sommer, P., (2005). The Pro-regions of lysyl oxidase and lysyl oxidase-like 1 are required for deposition onto elastic fibers. *J. Biol. Chem.*, **280**, 42848–42855.
[5]. Borel, A., Eichenberger, D., Farjanel, J., Kessler, E., Gleyzal, C., Hulmes, D.J., Sommer, P., Font, B., (2001). Lysyl oxidase-like protein from bovine aorta. Isolation and maturation to an active form by bone morphogenetic protein-1. *J. Biol. Chem.*, **276**, 48944–48949.
[6]. Liu, X., Zhao, Y., Gao, J., Pawlyk, B., Starcher, B., Spencer, J.A., Yanagisawa, H., Zuo, J., Li, T., (2004). Elastic fiber homeostasis requires lysyl oxidase-like 1 protein. *Nat. Genet.*, **36**, 178–182.
[7]. Kagan, H.M., Li, W., (2003). Lysyl oxidase: properties, specificity, and biological roles inside and outside of the cell. *J. Cell. Biochem.*, **88**, 660–672.
[8]. Nave, A.H., Mizikova, I., Niess, G., Steenbock, H., Reichenberger, F., Talavera, M.L., Veit, F., Herold, S., Mayer, K., Vadasz, I., Weissmann, N., Seeger, W., Brinckmann, J., Morty, R.E., (2014). Lysyl oxidases play a causal role in vascular remodeling in clinical and experimental pulmonary arterial hypertension. *Arterioscler. Thromb. Vasc. Biol.*, **34**, 1446–1458.
[9]. Tjin, G., White, E.S., Faiz, A., Sicard, D., Tschumperlin, D. J., Mahar, A., Kable, E.P.W., Burgess, J.K., (2017). Lysyl oxidases regulate fibrillar collagen remodelling in idiopathic pulmonary fibrosis. *Dis Model Mech.*, **10**, 1301–1312.
[10]. Zhou, Y., Ling, O., Bo, L., (2013). Expression and significance of lysyl oxidase-like 1 and fibulin-5 in the cardinal ligament tissue of patients with pelvic floor dysfunction. *J. Biomed. Res.*, **27**, 23–28.
[11]. Fingert, J.H., Alward, W.L., Kwon, Y.H., Wang, K., Streb, L.M., Sheffield, V.C., Stone, E.M., (2007). LOXL1 mutations are associated with exfoliation syndrome in patients from the midwestern United States. *Am. J. Ophthalmol.*, **144**, 974–975.
[12]. Aragon-Martin, J.A., Ritch, R., Liebmann, J., O'Brien, C., Blaaow, K., Mercieca, F., Spiteri, A., Cobb, C.J., Damji, K. F., Tarkkanen, A., Rezaie, T., Child, A.H., Sarfarazi, M., (2008). Evaluation of LOXL1 gene polymorphisms in exfoliation syndrome and exfoliation glaucoma. *Mol. Vis.*, **14**, 533–541.
[13]. Chen, L., Jia, L., Wang, N., Tang, G., Zhang, C., Fan, S., Liu, W., Meng, H., Zeng, W., Liu, N., Wang, H., Jia, H., (2009). Evaluation of LOXL1 polymorphisms in exfoliation syndrome in a Chinese population. *Mol Vis.*, **15**, 2349–2357.
[14]. Lemmela, S., Forsman, E., Onkamo, P., Nurmi, H., Laivuori, H., Kivela, T., Puska, P., Heger, M., Eriksson, A., Forsius, H., Jarvela, I., (2009). Association of LOXL1 gene with Finnish exfoliation syndrome patients. *J. Hum. Genet.*, **54**, 289–297.
[15]. Fan, B.J., Pasquale, L.R., Rhee, D., Li, T., Haines, J.L., Wiggs, J.L., (2011). LOXL1 promoter haplotypes are associated with exfoliation syndrome in a U.S. Caucasian population. *Invest. Ophthalmol. Vis. Sci.*, **52**, 2372–2378.
[16]. Rautenbach, R.M., Bardien, S., Harvey, J., Ziskind, A., (2011). An investigation into LOXL1 variants in black South African individuals with exfoliation syndrome. *Arch. Ophthalmol.*, **129**, 206–210.
[17]. Wirostko, B.M., Curtin, K., Ritch, R., Thomas, S., Allen-Brady, K., Smith, K.R., Hageman, G.S., Allingham, R.R., (2016). Risk for exfoliation syndrome in women with pelvic organ prolapse : a utah project on exfoliation syndrome (UPEXS) study. *JAMA Ophthalmol.*, **134**, 1255–1262.
[18]. Elhawy, E., Kamthan, G., Dong, C.Q., Danias, J., (2012). Pseudoexfoliation syndrome, a systemic disorder with ocular manifestations. *Hum Genomics.*, **6**, 22.
[19]. Ritch, R., Schlotzer-Schrehardt, U., (2001). Exfoliation syndrome. *Surv. Ophthalmol.*, **45**, 265–315.
[20]. Thorleifsson, G., Magnusson, K.P., Sulem, P., Walters, G.B., Gudbjartsson, D.F., Stefansson, H., Jonsson, T.,

Jonasdottir, A., Stefansdottir, G., Masson, G., Hardarson, G.A., Petursson, H., Arnarsson, A., Motallebipour, M., Wallerman, O., Wadelius, C., Gulcher, J.R., Thorsteinsdottir, U., Kong, A., Jonasson, F., Stefansson, K., (2007). Common sequence variants in the LOXL1 gene confer susceptibility to exfoliation glaucoma. *Science*, **317**, 1397–1400.

[21]. Jeng, S.M., Karger, R.A., Hodge, D.O., Burke, J.P., Johnson, D.H., Good, M.S., (2007). The risk of glaucoma in pseudoexfoliation syndrome. *J. Glaucoma*, **16**, 117–121.

[22]. Schlotzer-Schrehardt, U., Naumann, G.O., (2006). Ocular and systemic pseudoexfoliation syndrome. *Am. J. Ophthalmol.*, **141**, 921–937.

[23]. Boote, C., Sigal, I.A., Grytz, R., Hua, Y., Nguyen, T.D., Girard, M.J.A., (2020). Scleral structure and biomechanics. *Prog Retin Eye Res.*, **74**, 100773

[24]. Sigal, I.A., Ethier, C.R., (2009). Biomechanics of the optic nerve head. *Exp. Eye Res.*, **88**, 799–807.

[25]. Radius, R.L., Gonzales, M., (1981). Anatomy of the lamina cribrosa in human eyes. *Arch. Ophthalmol.*, **99**, 2159–2162.

[26]. Calkins, D.J., (2021). Adaptive responses to neurodegenerative stress in glaucoma. *Prog Retin Eye Res.*, **100953**

[27]. Burgoyne, C.F., (2011). A biomechanical paradigm for axonal insult within the optic nerve head in aging and glaucoma. *Exp. Eye Res.*, **93**, 120–132.

[28]. Sun, D., Lye-Barthel, M., Masland, R.H., Jakobs, T.C., (2009). The morphology and spatial arrangement of astrocytes in the optic nerve head of the mouse. *J. Comp. Neurol.*, **516**, 1–19.

[29]. Quillen, S., Schaub, J., Quigley, H., Pease, M., Korneva, A., Kimball, E., (2020). Astrocyte responses to experimental glaucoma in mouse optic nerve head. *PLoS ONE*, **15**, e0238104.

[30]. Keeley, F.W., Morin, J.D., Vesely, S., (1984). Characterization of collagen from normal human sclera. *Exp. Eye Res.*, **39**, 533–542.

[31]. Thale, A., Tillmann, B., (1993). The collagen architecture of the sclera–SEM and immunohistochemical studies. *Ann Anat.*, **175**, 215–220.

[32]. Summers Rada, J.A., Shelton, S., Norton, T.T., (2006). The sclera and myopia. *Exp. Eye Res.*, **82**, 185–200.

[33]. Quigley, H.A., Dorman-Pease, M.E., Brown, A.E., (1991). Quantitative study of collagen and elastin of the optic nerve head and sclera in human and experimental monkey glaucoma. *Curr. Eye Res.*, **10**, 877–888.

[34]. Marshall, G.E., (1995). Human scleral elastic system: an immunoelectron microscopic study. *Br. J. Ophthalmol.*, **79**, 57–64.

[35]. Albon, J., Karwatowski, W.S., Avery, N., Easty, D.L., Duance, V.C., (1995). Changes in the collagenous matrix of the aging human lamina cribrosa. *Br. J. Ophthalmol.*, **79**, 368–375.

[36]. Hernandez, M.R., Luo, X.X., Andrzejewska, W., Neufeld, A.H., (1989). Age-related changes in the extracellular matrix of the human optic nerve head. *Am. J. Ophthalmol.*, **107**, 476–484.

[37]. Morrison, J.C., Jerdan, J.A., Dorman, M.E., Quigley, H.A., (1989). Structural proteins of the neonatal and adult lamina cribrosa. *Arch. Ophthalmol.*, **107**, 1220–1224.

[38]. Quigley, H.A., Addicks, E.M., (1981). Regional differences in the structure of the lamina cribrosa and their relation to glaucomatous optic nerve damage. *Arch. Ophthalmol.*, **99**, 137–143.

[39]. De Maria, A., Wilmarth, P.A., David, L.L., Bassnett, S., (2017). Proteomic Analysis of the Bovine and Human Ciliary Zonule. *Invest. Ophthalmol. Vis. Sci.*, **58**, 573–585.

[40]. Teekhasaenee C. Current concepts in true exfoliation syndrome. *Journal of Glaucoma*. 2018;27:S105-S110.

[41]. Ozcura, F., Aydin, S., Dayanir, V., (2011). Central corneal thickness and corneal curvature in pseudoexfoliation syndrome with and without glaucoma. *J. Glaucoma*, **20**, 410–413.

[42]. Wiggs, J.L., Pawlyk, B., Connolly, E., Adamian, M., Miller, J.W., Pasquale, L.R., Haddadin, R.I., Grosskreutz, C.L., Rhee, D.J., Li, T., (2014). Disruption of the blood-aqueous barrier and lens abnormalities in mice lacking lysyl oxidase-like 1 (LOXL1). *Invest. Ophthalmol. Vis. Sci.*, **55**, 856–864.

[43]. Li, G., Schmitt, H., Johnson, W.M., Lee, C., Navarro, I., Cui, J., Fleming, T., Gomez-Caraballo, M., Elliott, M.H., Sherwood, J.M., Hauser, M.A., Farsiu, S., Ethier, C.R., Stamer, W.D., (2020). Integral role for lysyl oxidase-like-1 in conventional outflow tissue function and behavior. *FASEB J.*, **34**, 10762–10777.

[44]. Savinova, O.V., Sugiyama, F., Martin, J.E., Tomarev, S.I., Paigen, B.J., Smith, R.S., John, S.W., (2001). Intraocular pressure in genetically distinct mice: an update and strain survey. *BMC Genet.*, **2**, 12.

[45]. Camras, L.J., Sufficool, K.E., Camras, C.B., Fan, S., Liu, H., Toris, C.B., (2010). Duration of anesthesia affects intraocular pressure, but not outflow facility in mice. *Curr. Eye Res.*, **35**, 819–827.

[46]. Cone, F.E., Steinhart, M.R., Oglesby, E.N., Kalesnykas, G., Pease, M.E., Quigley, H.A., (2012). The effects of anesthesia, mouse strain and age on intraocular pressure and an improved murine model of experimental glaucoma. *Exp. Eye Res.*, **99**, 27–35.

[47]. Wu HJ, Hazlewood RJ, Kuchtey J and Kuchtey RW. Enlarged Optic Nerve Axons and Reduced Visual Function in Mice with Defective Microfibrils. *eNeuro*. 2018;5.

[48]. Liu, X., Zhao, Y., Pawlyk, B., Damaser, M., Li, T., (2006). Failure of elastic fiber homeostasis leads to pelvic floor disorders. *Am. J. Pathol.*, **168**, 519–528.

[49]. Couri, B.M., Borazjani, A., Lenis, A.T., Balog, B., Kuang, M., Lin, D.L., Damaser, M.S., (2014). Validation of genetically matched wild-type strain and lysyl oxidase-like 1 knockout mouse model of pelvic organ prolapse. *Female Pelvic Med Reconstr Surg.*, **20**, 287–292.

[50]. Markov, P.P., Eliasy, A., Pijanka, J.K., Htoon, H.M., Paterson, N.G., Sorensen, T., Elsheikh, A., Girard, M.J.A., Boote, C., (2018). Bulk changes in posterior scleral collagen microstructure in human high myopia. *Mol. Vis.*, **24**, 818–833.

[51]. Wang, B., Hua, Y., Brazile, B.L., Yang, B., Sigal, I.A., (2020). Collagen fiber interweaving is central to sclera stiffness. *Acta Biomater.*, **113**, 429–437.

[52]. Ismail, E.N., Ruberti, J.W., Malek, G., (2017). Quick-freeze/deep-etch electron microscopy visualization of the mouse posterior pole. *Exp. Eye Res.*, **162**, 62–72.

[53]. Siegel, R.C., Pinnell, S.R., Martin, G.R., (1970). Cross-linking of collagen and elastin. Properties of lysyl oxidase. *Biochemistry*, **9**, 4486–4492.

[54]. Toris, C.B., Yablonski, M.E., Wang, Y.L., Camras, C.B., (1999). Aqueous humor dynamics in the aging human eye. *Am. J. Ophthalmol.*, **127**, 407–412.

[55]. Gabelt, B.T., Kaufman, P.L., (2005). Changes in aqueous humor dynamics with age and glaucoma. *Prog Retin Eye Res.*, **24**, 612–637.
[56]. Tamm, E.R., (2009). The trabecular meshwork outflow pathways: structural and functional aspects. *Exp. Eye Res.*, **88**, 648–655.
[57]. Qiu, Y., Yang, H., Lei, B., (2014). Effects of three commonly used anesthetics on intraocular pressure in mouse. *Curr. Eye Res.*, **39**, 365–369.
[58]. Nathan, N., Kuchtey, R.W., (2016). Genetics, diagnosis, and monitoring of pseudoexfoliation glaucoma. *Curr Ophthalmol Rep.*, **4**, 206–212.
[59]. De Maria, A., Zientek, K.D., David, L.L., Wilmarth, P.A., Bhorade, A.M., Harocopos, G.J., Huang, A.J.W., Hong, A. R., Siegfried, C.J., Tsai, L.M., Sheybani, A., Bassnett, S., (2021). Compositional analysis of extracellular aggregates in the eyes of patients with exfoliation syndrome and exfoliation glaucoma. *Invest. Ophthalmol. Vis. Sci.*, **62**, 27.
[60]. Goldfischer, S., Coltoff-Schiller, B., Goldfischer, M., (1985). Microfibrils, elastic anchoring components of the extracellular matrix, are associated with fibronectin in the zonule of Zinn and aorta. *Tissue Cell*, **17**, 441–450.
[61]. Feola, A.J., Myers, J.G., Raykin, J., Mulugeta, L., Nelson, E.S., Samuels, B.C., Ethier, C.R., (2016). Finite element modeling of factors influencing optic nerve head deformation due to intracranial pressure. *Invest. Ophthalmol. Vis. Sci.*, **57**, 1901–1911.
[62]. Hua, Y., Tong, J., Ghate, D., Kedar, S., Gu, L., (2017). Intracranial pressure influences the behavior of the optic nerve head. *J. Biomech. Eng.*, **139**
[63]. Curtin, B.J., Iwamoto, T., Renaldo, D.P., (1979). Normal and staphylomatous sclera of high myopia. An electron microscopic study. *Arch Ophthalmol.*, **97**, 912–915.
[64]. Cone, F.E., Gelman, S.E., Son, J.L., Pease, M.E., Quigley, H.A., (2010). Differential susceptibility to experimental glaucoma among 3 mouse strains using bead and viscoelastic injection. *Exp. Eye Res.*, **91**, 415–424.
[65]. Gelman, S., Cone, F.E., Pease, M.E., Nguyen, T.D., Myers, K., Quigley, H.A., (2010). The presence and distribution of elastin in the posterior and retrobulbar regions of the mouse eye. *Exp. Eye Res.*, **90**, 210–215.
[66]. Zhao, W., Yang, A., Chen, W., Wang, P., Liu, T., Cong, M., Xu, A., Yan, X., Jia, J., You, H., (2018). Inhibition of lysyl oxidase-like 1 (LOXL1) expression arrests liver fibrosis progression in cirrhosis by reducing elastin crosslinking. *Biochim. Biophys. Acta, Mol. Basis Dis.*, **1864**, 1129–1137.
[67]. Jameson, S.A., Swaminathan, G., Dahal, S., Couri, B., Kuang, M., Rietsch, A., Butler, R.S., Ramamurthi, A., Damaser, M.S., (2020). Elastin homeostasis is altered with pelvic organ prolapse in cultures of vaginal cells from a lysyl oxidase-like 1 knockout mouse model. *Physiol. Rep.*, **8**, e14436.
[68]. Pijanka, J.K., Spang, M.T., Sorensen, T., Liu, J., Nguyen, T.D., Quigley, H.A., Boote, C., (2015). Depth-dependent changes in collagen organization in the human peripapillary sclera. *PLoS ONE*, **10**, e0118648.
[69]. Aoki, C., Uto, K., Honda, K., Kato, Y., Oda, H., (2013). Advanced glycation end products suppress lysyl oxidase and induce bone collagen degradation in a rat model of renal osteodystrophy. *Lab. Invest.*, **93**, 1170–1183.
[70]. Herchenhan, A., Uhlenbrock, F., Eliasson, P., Weis, M., Eyre, D., Kadler, K.E., Magnusson, S.P., Kjaer, M., (2015). Lysyl oxidase activity is required for ordered collagen fibrillogenesis by tendon cells. *J. Biol. Chem.*, **290**, 16440–16450.
[71]. Canelon, S.P., Wallace, J.M., (2016). Beta-aminopropionitrile-induced reduction in enzymatic crosslinking causes in vitro changes in collagen morphology and molecular composition. *PLoS ONE*, **11**, e0166392.
[72]. Revell, C.K., Jensen, O.E., Shearer, T., Lu, Y., Holmes, D.F., Kadler, K.E., (2021). Collagen fibril assembly: New approaches to unanswered questions. *Matrix Biol. Plus*, **12**, 100079
[73]. Komai, Y., Ushiki, T., (1991). The three-dimensional organization of collagen fibrils in the human cornea and sclera. *Invest. Ophthalmol. Vis. Sci.*, **32**, 2244–2258.
[74]. Coudrillier, B., Pijanka, J., Jefferys, J., Sorensen, T., Quigley, H.A., Boote, C., Nguyen, T.D., (2015). Collagen structure and mechanical properties of the human sclera: analysis for the effects of age. *J. Biomech. Eng.*, **137**, 041006
[75]. Guimarães, C.F., Gasperini, L., Marques, A.P., Reis, R. L., (2020). The stiffness of living tissues and its implications for tissue engineering. *Nat. Rev. Mater.*, **5**, 351–370.
[76]. Ryan, A.J., O'Brien, F.J., (2015). Insoluble elastin reduces collagen scaffold stiffness, improves viscoelastic properties, and induces a contractile phenotype in smooth muscle cells. *Biomaterials*, **73**, 296–307.
[77]. Ahmadzadeh, H., Connizzo, B.K., Freedman, B.R., Soslowsky, L.J., Shenoy, V.B., (2013). Determining the contribution of glycosaminoglycans to tendon mechanical properties with a modified shear-lag model. *J. Biomech.*, **46**, 2497–2503.
[78]. Kim, T., Sridharan, I., Ma, Y., Zhu, B., Chi, N., Kobak, W., Rotmensch, J., Schieber, J.D., Wang, R., (2016). Identifying distinct nanoscopic features of native collagen fibrils towards early diagnosis of pelvic organ prolapse. *Nanomedicine*, **12**, 667–675.
[79]. Siegwart Jr., J.T., Norton, T.T., (1999). Regulation of the mechanical properties of tree shrew sclera by the visual environment. *Vision Res.*, **39**, 387–407.
[80]. Avetisov, E.S., Savitskaya, N.F., Vinetskaya, M.I., Iomdina, E.N., (1983). A study of biochemical and biomechanical qualities of normal and myopic eye sclera in humans of different age groups. *Metab. Pediatr. Syst. Ophthalmol.*, **7**, 183–188.
[81]. Friberg, T.R., Lace, J.W., (1988). A comparison of the elastic properties of human choroid and sclera. *Exp. Eye Res.*, **47**, 429–436.
[82]. Bailey, A.J., Paul, R.G., Knott, L., (1998). Mechanisms of maturation and ageing of collagen. *Mech. Ageing Dev.*, **106**, 1–56.
[83]. Schultz, D.S., Lotz, J.C., Lee, S.M., Trinidad, M.L., Stewart, J.M., (2008). Structural factors that mediate scleral stiffness. *Invest. Ophthalmol. Vis. Sci.*, **49**, 4232–4236.
[84]. Eilaghi, A., Flanagan, J.G., Simmons, C.A., Ethier, C.R., (2010). Effects of scleral stiffness properties on optic nerve head biomechanics. *Ann. Biomed. Eng.*, **38**, 1586–1592.
[85]. Braunsmann, C., Hammer, C.M., Rheinlaender, J., Kruse, F.E., Schaffer, T.E., Schlotzer-Schrehardt, U., (2012).

Evaluation of lamina cribrosa and peripapillary sclera stiffness in pseudoexfoliation and normal eyes by atomic force microscopy. *Invest. Ophthalmol. Vis. Sci.*, **53**, 2960–2967.

[86]. Grytz, R., Yang, H., Hua, Y., Samuels, B.C., Sigal, I.A., (2020). Connective tissue remodeling in myopia and its potential role in increasing risk of glaucoma. *Curr. Opin. Biomed. Eng.*, **15**, 40–50.

[87]. Kimball, E.C., Nguyen, C., Steinhart, M.R., Nguyen, T.D., Pease, M.E., Oglesby, E.N., Oveson, B.C., Quigley, H.A., (2014). Experimental scleral cross-linking increases glaucoma damage in a mouse model. *Exp. Eye Res.*, **128**, 129–140.

[88]. Hannon, B.G., Luna, C., Feola, A.J., Ritch, M.D., Read, A. T., Stinnett, S.S., Vo, H., Pardue, M.T., Gonzalez, P., Ethier, C.R., (2020). Assessment of visual and retinal function following in vivo genipin-induced scleral crosslinking. *Transl. Vis. Sci. Technol.*, **9**, 8.

[89]. Wu, H.J., Mortlock, D.P., Kuchtey, R.W., Kuchtey, J., (2021). Altered ocular fibrillin microfibril composition in mice with a glaucoma-causing mutation of adamts10. *Invest. Ophthalmol. Vis. Sci.*, **62**, 26.

[90]. Koehn, D., Meyer, K.J., Syed, N.A., Anderson, M.G., (2015). Ketamine/xylazine-induced corneal damage in mice. *PLoS ONE*, **10**, e0132804.

[91]. Sadun, A.A., Smith, L.E., Kenyon, K.R., (1983). Paraphenylenediamine: a new method for tracing human visual pathways. *J. Neuropathol. Exp. Neurol.*, **42**, 200–206.

[92]. Sun, W.W., Krystofiak, E.S., Leo-Macias, A., Cui, R., Sesso, A., Weigert, R., Ebrahim, S., Kachar, B., (2020). Nanoarchitecture and dynamics of the mouse enteric glycocalyx examined by freeze-etching electron tomography and intravital microscopy. *Commun Biol.*, **3**, 5.

[93]. Schindelin, J., Arganda-Carreras, I., Frise, E., Kaynig, V., Longair, M., Pietzsch, T., Preibisch, S., Rueden, C., Saalfeld, S., Schmid, B., Tinevez, J.-Y., White, D.J., Hartenstein, V., Eliceiri, K., Tomancak, P., Cardona, A., (2012). Fiji: an open-source platform for biological-image analysis. *Nat. Methods*, **9**, 676–682.

[94]. Morgan, J.T., Raghunathan, V.K., Thomasy, S.M., Murphy, C.J., Russell, P., (2014). Robust and artifact-free mounting of tissue samples for atomic force microscopy. *Biotechniques*, **56**, 40–42.